

# Star Formation Triggered by Supernova Explosions in Young Galaxies

Takanori Nagakura<sup>1\*</sup>, Takashi Hosokawa<sup>1</sup>, and Kazuyuki Omukai<sup>1</sup>

<sup>1</sup>National Astronomical Observatory of Japan, Osawa, Mitaka, Tokyo 181-8588

13 August 2018

## ABSTRACT

We study the evolution of supernova remnants in a low-metallicity medium  $Z/Z_{\odot} = 10^{-4} - 10^{-2}$  in the early universe, using one-dimensional hydrodynamics with non-equilibrium chemistry. Once a post-shock layer is able to cool radiatively, a dense shell forms behind the shock. If this shell becomes gravitationally unstable and fragments into pieces, next-generation stars are expected to form from these fragments. To explore the possibility of this triggered star formation, we apply a linear perturbation analysis of an expanding shell to our results and constrain the parameter range of ambient density, explosion energy, and metallicity where fragmentation of the shell occurs. For the explosion energy of  $10^{51}$  ergs ( $10^{52}$  ergs), the shell fragmentation occurs for ambient densities higher than  $\gtrsim 10^2 \text{ cm}^{-3}$  ( $10 \text{ cm}^{-3}$ , respectively). This condition depends little on the metallicity in the ranges we examined. We find that the mode of star formation triggered occurs only in massive ( $\gtrsim 10^8 M_{\odot}$ ) haloes.

**Key words:** cosmology:theory – galaxies:formation – high-redshift – ISM:supernova remnants – shock waves – stars:formation

## 1 INTRODUCTION

Understanding of star formation and its feedback effects in the high-redshift universe is a key to unravelling how the primeval universe has evolved into the variety of luminous objects we observe today. Recent numerical studies have indicated that the first stars, or Pop III.1 stars (O’Shea et al. 2008), presumably have typical mass of  $\gtrsim 100 M_{\odot}$  (Abel, Bryan & Norman 2002; Bromm, Coppi & Larson 2002; Omukai & Palla 2003; Yoshida et al. 2006). Copious amounts of radiation from such very massive stars photo-ionize hydrogen atoms and photo-dissociate molecular hydrogen in their surroundings (Kitayama et al. 2004; Whalen et al. 2004). As well as the radiative feedback, the first star deaths have an impact on subsequent star formation around them. The ultimate fate of metal-free stars is determined by their mass. Stellar evolution models predict that stars with  $40 - 140 M_{\odot}$  finally collapse into black holes without supernovae, while those with  $10 - 40 M_{\odot}$  or  $140 - 260 M_{\odot}$  explode as Type II supernovae or pair-instability supernovae (PISNe), respectively (Heger & Woosley 2002; Umeda & Nomoto 2002).

If the first star dies without supernova, the HII region is left over around a remnant black hole. At the centre of the fossil HII region,  $\text{H}_2$  is quickly replenished owing to a large amount of electrons, which are the catalysts for the  $\text{H}_2$  formation reaction. The resultant fast radiative cooling allows a small portion of the gas to re-collapse and turn into the next-generation stars, provided that no ex-

ternal ultraviolet (UV) radiation effectively dissociates  $\text{H}_2$  and the dark halo mass is higher than  $10^5 M_{\odot}$  (Nagakura & Omukai 2005). In addition, deuterated hydrogen (HD) molecules abundantly form in such regions and further reduce the gas temperature to that of the CMB. The re-collapsing gas fragments with typical mass of  $\simeq 40 M_{\odot}$  (Yoshida et al. 2007), which is an order of magnitude lower than that of the first stars (see also, Uehara & Inutsuka 2000; Nakamura & Umemura 2002).

If the first star explodes as a supernova, the surrounding medium is severely affected by the blast wave. The blast wave removes most of the gas from a low-mass halo ( $\lesssim 10^6 M_{\odot}$ ) even for the explosion energy as low as  $10^{50}$  erg (Kitayama & Yoshida 2005; Whalen et al. 2008), because the gas density has been decreased to  $0.1 - 1 \text{ cm}^{-3}$  inside the HII region. Evacuation of the gas from the halo quenches subsequent star formation in the same halo without a substantial gas supply through merging with other haloes (Greif et al. 2007). For a supernova in higher-mass haloes ( $\gtrsim 10^7 M_{\odot}$ ), the situations are quite different. The halo gas remains in the HII region owing to a deeper dark matter potential well (Kitayama et al. 2004). The blast wave stagnates inside the halo and sweeps a considerable amount of gas into a dense shell (Whalen et al. 2008). Such a shell is a potential site for next-generation star formation. The stability analyses of linear perturbations on an expanding and decelerating thin shell predict that small density perturbations can grow to trigger gravitational instabilities, provided that the temperature in the shell becomes low enough and sufficient gas is taken into the shell (Elmegreen 1994; Whitworth et al. 1994). Some authors have investigated the possibility of star formation triggered by the first supernova explosions (Ferrara 1998; Mackey, Bromm

\* E-mail: nagakura@th.nao.ac.jp (TN) ; hosokawa@th.nao.ac.jp (TH) ; omukai@th.nao.ac.jp (KO)

& Hernquist 2003; Bromm, Yoshida & Hernquist 2003; Salvaterra, Ferrara & Schneider 2004; Machida et al. 2005; Vasiliev, Vorobyov & Shchekinov 2008; Whalen et al. 2008). Applying a classical supernova remnant (SNR) model to a primordial gas, Salvaterra et al. (2004) and Machida et al. (2005) found the combination of the explosion energy and the ambient density where the shell fragmentation occurs, and discussed the typical mass of the stars forming in the shell. However, their results are somewhat different because of different one-zone modelling. To solve this uncertainty, more detailed calculation is needed.

Supernovae also disperse heavy elements into the intergalactic medium (IGM) (e.g., Kitayama & Yoshida 2005). Greif et al. (2007) showed that the metals are preferentially transferred into voids, while some of them collide with neighbouring haloes and mix with the gas in them through hydrodynamical instabilities such as Kelvin-Helmholtz instability. Cen & Riquelme (2008) showed that the mixing occurs only at the edge of haloes of  $10^{6-7} M_{\odot}$  at  $z = 10$ . However, irradiation of ionizing photons from neighbouring haloes, which was omitted from their analysis, may enhance the metal enrichment of lower-mass haloes at higher redshifts. Turbulent motions excited by hierarchical mergers also causes the efficient metal mixing (Wise & Abel 2007; Grief et al. 2008). Metals contribute to the radiative cooling of gas, having an effect on dynamical evolution of SNRs. Thornton et al. (1998) investigated this issue for a wide metallicity range with the intention of including the SN feedback in galaxy-formation simulations. They showed that the metal cooling modifies the redistribution of supernova energy to the surroundings for metallicity  $> 0.01Z_{\odot}$ . However, they paid no attention to the structure and evolution of the supernova-driven shell nor to the possibility of subsequent fragmentation.

The aim of this paper is to find the condition where the supernova-driven shell fragments and triggers subsequent star formation in young galaxies. Towards this end, we study the evolution of supernova remnants in the low-metallicity interstellar medium by way of hydrodynamics with spherical symmetry. This paper is organized as follows: In Section 2, we describe the numerical method and input physics. The results are presented in Section 3, where we first describe dynamical evolution of an SNR and the structure of the shell, focusing on the roles of metals, and then discuss the possibility of the shell fragmentation using the linear stability analysis by Elmegreen (1994). In Section 4, by using the above result, we constrain the mass range of haloes where the triggered star formation occurs. In addition, we discuss effects of processes not included in our analysis. Finally, we summarize our study in Section 5. Throughout this paper, we adopt a flat  $\Lambda$ CDM model with parameters  $\Omega_{\Lambda} = 0.73$ ,  $\Omega_m = 0.27$ ,  $\Omega_b = 0.044$ , and Hubble parameter  $h = 0.71$  (Spergel et al. 2003).

## 2 THE MODEL

### 2.1 Hydrodynamics and Chemistry

We solve the following basis equations for one-dimensional hydrodynamics with spherical symmetry:

$$\frac{\partial \rho}{\partial t} + \frac{1}{r^2} \frac{\partial}{\partial r}(\rho v) = 0, \quad (1)$$

$$\frac{\partial v}{\partial t} + v \frac{\partial v}{\partial r} = -\frac{1}{\rho} \frac{\partial p}{\partial r} - \frac{Gm(r)}{r^2}, \quad (2)$$

$$\begin{aligned} \frac{\partial}{\partial t}(\rho e) + \frac{1}{r^2} \frac{\partial}{\partial r}(r^2 \rho e v) + \frac{p}{r^2} \frac{\partial}{\partial r}(r^2 v) \\ = -\Lambda(\rho, T) + \frac{1}{r^2} \frac{\partial}{\partial r} \left[ \kappa(T) r^2 \frac{\partial T}{\partial r} \right], \end{aligned} \quad (3)$$

$$p = (\gamma - 1)\rho e = \frac{k_B T}{\mu m_H} \rho, \quad (4)$$

where  $\rho$  is the mass density of the gas,  $v$  the velocity of the fluid elements,  $p$  the pressure,  $e$  the internal energy per unit mass,  $m(r)$  the enclosed mass within the radius  $r$ ,  $\gamma$  the adiabatic exponent,  $\mu$  the mean molecular weight,  $m_H$  the mass of a hydrogen atom,  $\Lambda$  the radiative cooling rate per unit volume and time,  $k_B$  the Boltzmann's constant, and  $\kappa(T)$  the thermal conductivity. The thermal conductivity is the sum of contributions from atomic diffusion at low temperatures (Parker 1953) and electronic diffusion at high temperatures (Spitzer 1962; Cowie & McKee 1977). In our calculations, a cooling layer behind a shock driven by a supernova becomes thermally unstable for wavelengths shorter than a so-called Field length (Field 1965):  $\lambda_F = (\kappa T / \Lambda)^{1/2}$ . Thermal conduction tends to curtail the thermal instability, but the Field length is many orders of magnitude shorter than a characteristic length (e.g., a radius of an SNR). The limitation of our simulation resources makes it difficult to resolve the Field length. To suppress unphysical oscillations due to the thermal instability occurring below the spatial resolution limit, we temporarily enhance the thermal conductivity only for the thermally unstable cooling layer at the incipient stage of the shell formation (see Hosokawa & Inutsuka 2006). This prescription smoothes the temperature structure out on the newly defined Field length, but does not significantly alter the thermal evolution of the shell because the Field length is still shorter than the scale-length of temperature variation.

The hydrodynamics are solved with a second-order Godunov method in the Lagrangian coordinate (van Leer 1979). We split the gas into fluid elements which are unequal in mass such that more fluid elements exist in the post-shock regions. We set the number of the total fluid elements to 1000 and choose a simulation box of length 100 – 1000 pc, depending on the explosion energy and the ambient density. We have confirmed that the results do not change when the total number of mesh points is doubled. To check the accuracy of our code, we have carried out a test simulation on a dynamical expansion of a point-source explosion without any dissipative processes and ascertained that the result is excellently consistent with the Sedov-Taylor solution.

Along with the hydrodynamics, we solve a set of kinetic equations for chemical species. We include 15 primordial components and 4 heavy elements as follows: H, H<sup>+</sup>, H<sup>-</sup>, H<sub>2</sub>, H<sub>2</sub><sup>+</sup>, HeH<sup>+</sup>, He, He<sup>+</sup>, He<sup>++</sup>, e<sup>-</sup>, D, D<sup>+</sup>, D<sup>-</sup>, HD, HD<sup>+</sup>, C, C<sup>+</sup>, O, and O<sup>+</sup>.

The kinetic equation for the  $i$ -th species is

$$\begin{aligned} \frac{dy(i)}{dt} = & -n_{\text{H}}y(i) \sum_j k_{ij}y(j) + n_{\text{H}} \sum_{lm} k_{lm}y(l)y(m) \\ & + n_{\text{H}}^2 \sum_{ijk} k_{ijk}y(i)y(j)y(k), \end{aligned} \quad (5)$$

where  $n_{\text{H}}$  is the number density of hydrogen nuclei,  $y(i)$  the fraction of the number density for the  $i$ -th chemical species to  $n_{\text{H}}$ ,  $k_{ij}$  and  $k_{lm}$  the destruction and the formation rate of  $y(i)$ , respectively, and  $k_{ijk}$  the reaction rates for three-body reactions. We include 53 reactions among these species on the basis of the minimum model suggested by Omukai et al. (2005) and listed in Table A1. The primordial chemical networks are based on Abel et al. (1997) and Galli & Palla (1998). The reactions involved with carbon and oxygen are the recombination of  $\text{C}^+$  (reaction [R42]) and  $\text{O}^+$  (reaction [R43]). In addition, we incorporate the charge exchange reactions between H and  $\text{O}^+$  (reaction [R44]), and between  $\text{H}^+$  and O (reaction [R45]) because these reactions occur quickly due to a slight difference among their ionization potentials. We do not take into account the charge exchange reactions between C and  $\text{H}^+$  or between H and  $\text{C}^+$  because these reactions are much less important than reactions [R44] and [R45] (Glover & Jappsen 2007). Although the emissions from the compounds of carbon or oxygen such as OH, and  $\text{H}_2\text{O}$  slightly contribute to the total radiative cooling at densities ranging from  $10^5 \text{ cm}^{-3}$  to  $10^{10} \text{ cm}^{-3}$  (see, Omukai et al. 2005), we omit the reactions among them because they have only minor effects in the density range we explored. We apply the set of equations to each fluid element and solve them with an implicit scheme because of the stiffness of these equations. The adopted time steps are actually shorter than the chemical time. We implicitly solve the chemical reactions to make sure the numerical stability. We have confirmed that our results do not change even with the shorter time steps.

## 2.2 Radiative Processes

The net cooling rate  $\Lambda$  in equation (3) is the sum of the contributions from radiative cooling processes. In simulating supernova explosions, we need to treat both the hot interior bubble and dense shell driven by the blast wave. The temperature range is wide, spanning a wide range from 10 K to  $10^9$  K. In the high-temperature regime of  $> 10^4$  K, the important processes include thermal bremsstrahlung emission, inverse Compton scattering of the CMB, collisional ionization and excitation of hydrogen and helium atoms, recombination of hydrogen and helium. Their cooling rates are taken from Cen (1992). On the other hand, at lower temperatures, the radiative processes by molecules and metals become important. We take account of  $\text{H}_2$  and HD ro-vibrational cooling (Hollenbach & McKee 1979; Galli & Palla 1998). Recently, Glover & Abel (2008) have computed new  $\text{H}_2$  cooling rates for  $e^- - \text{H}_2$  and  $\text{H}^+ - \text{H}_2$  collision channels in addition to the rate we included. We do not include these updated rates for simplicity. This effect might slightly reduce temperature of the post-shock gas, but not affect our conclusions. We also include the meta-stable and fine-structure line cooling by carbon and oxygen (Hollenbach & McKee 1989): [C I] $\lambda$ 9823,  $\lambda$ 4622, and  $\lambda$ 8727; [C II] $\lambda$ 2326; [O I] $\lambda$ 6300,  $\lambda$ 2972, and  $\lambda$ 5577; [O II] $\lambda$ 3729, 3726, and 508  $\mu\text{m}$ ; [C I]609.2 $\mu\text{m}$ , 229.9 $\mu\text{m}$ , and 369.0 $\mu\text{m}$ ; [O I]63.1 $\mu\text{m}$ , 44.2 $\mu\text{m}$ , and 145.6 $\mu\text{m}$ . The cooling rates are derived by solving the statistical equilibrium between the energy levels. We omit the metal line cooling at temperatures higher than  $10^4$  K because its contribution

is less important in the metallicity range we consider (see, Sutherland & Dopita 1993).

Some metals are expected to have condensed into dust grains even in the early universe (Nozawa et al. 2003; Bianchi & Schneider 2007). The dust can be an efficient radiator, but it is important only at densities far higher than we consider here. Also, it plays a role in a heating source through photo-electric heating under a strong radiation field. This rate depends on the properties of the radiation field as well as dust grains, both of which are quite uncertain in the high-redshift universe. Here, we just omit the dust effect for simplicity.

The CMB temperature is quite a high value of  $\sim 44$  K at  $z \sim 15$ . If a gas temperature decreases below that of the CMB, the CMB photons heat the gas through radiative pumping. This effect is taken into consideration in our calculation. We do not include other heating such as cosmic rays or external radiation from other sources.

## 2.3 Initial Condition

Before the supernova explosion, the progenitor star ionizes the surrounding medium. Dynamical expansion of the HII region has been investigated by several authors (Whalen et al. 2004; Kitayama et al. 2004; Hosokawa & Inutsuka 2006). A shock wave associated with the ionization front pushes a large amount of the circumstellar gas away, leveling the density off. Thus, we simply assume that the surrounding gas is homogeneous and fully ionized at temperature  $10^4$  K. In reality, the typical temperature in HII regions around Population III stars is somewhat higher than  $10^4$  K (Whalen et al. 2004; Kitayama et al. 2004). However, this difference will not be so significant in our calculations. In an early phase of the expansion, ambient thermal pressure is negligible compared with ram pressure exerted on the shell. Temperature in the fossil HII regions quickly falls below  $10^4$  K by the Lyman- $\alpha$  cooling. The initial temperature difference will be wiped out before the ambient thermal pressure acts to decelerate the shell. The ambient density depends on the conditions of formation sites of the progenitors. Here, we treat it as a free parameter and study the cases of  $n_0 = 0.1, 1, 10$ , and  $10^3 \text{ cm}^{-3}$ . We start the simulations at redshift  $z = 15$ .

We inject the supernova energy  $E_{\text{SN}}$  in the form of thermal energy and load the ejecta mass into several central meshes. Since the explosion energy can differ from event to event, we studied the three cases of  $E_{\text{SN}} = 10^{51}, 10^{52}$  and  $10^{53}$  ergs, which correspond to normal core-collapse supernovae, hypernovae and PISNe, respectively. Note that we performed the PISN runs only for low-metallicity ( $Z = 10^{-4} Z_{\odot}$ ) because metal enrichment reduces a typical fragment scale of a collapsing gas, and hence stellar mass (e.g., Omukai et al. 2005). The result depends little on the ejecta mass because it is much smaller than the mass swept up later into the shell. Hence, we simply fix it to  $10 M_{\odot}$ .

For the elemental abundances in ISM, the number fractions of He and D nuclei to the hydrogen ones are  $7.9 \times 10^{-2}$  and  $2.5 \times 10^{-5}$  respectively. We study the cases with metallicities  $Z/Z_{\odot} = 10^{-4}, 10^{-3}, 10^{-2}$ . For simplicity, we assume the metal abundance ratios are in proportion to the solar values. The number fractions of carbon and oxygen are  $3.6 \times 10^{-4}$  and  $8.5 \times 10^{-4}$ , respectively, for the solar metallicity (Anders & Grevesse 1989).

### 3 RESULTS

#### 3.1 Dynamical Expansion of a Supernova Remnant

We first present the result for the parameter set of  $E_{\text{SN}} = 10^{52}$  erg,  $n_0 = 1 \text{ cm}^{-3}$ , and  $Z = 10^{-4} Z_{\odot}$ , which we hereafter call the fiducial run. Fig. 1 shows the snapshots of (a) the density, (b) temperature, (c) pressure, and (d) velocity distribution as a function of the radius. The numbers in Fig. 1 represent the structures at time (1)  $9.0 \times 10^3$ , (2)  $4.8 \times 10^4$ , (3)  $1.7 \times 10^5$ , (4)  $4.9 \times 10^5$ , (5)  $1.1 \times 10^6$ , (6)  $5.0 \times 10^6$ , and (7)  $1.0 \times 10^7$  yr. A contact discontinuity forms quite early at the boundary between the stellar remnants and the surrounding medium, which is consistent with the previous studies (Chevalier 1974; Cioffi, McKee & Bertschinger 1988; Thornton et al. 1998). However, this discontinuity disappears before the state (1) because the heat transfer causes the gas slightly outside it to flow into a hot interior bubble while smoothing out the boundary. The strong shock evolves adiabatically until  $t = 8.5 \times 10^4$  yr. The post-shock density is  $(\gamma + 1)/(\gamma - 1) = 4$  times as high as that of the ambient medium. The shock front moves outwards in conformity with the canonical power-law form;  $R_{\text{sh}} \propto t^{\eta}$ , where the exponent  $\eta = 2/5$  during the Sedov-Taylor (ST) phase.

The expansion time of the shock front,  $R_{\text{sh}}/\dot{R}_{\text{sh}}$ , increases linearly with the time elapsed during the ST phase, while the radiative cooling time in the post-shock layer,  $\rho e/\Lambda$ , continues to decrease. After the cooling time becomes shorter than the expansion time at  $t = 8.5 \times 10^4$  yr, the post-shock temperature quickly plunges to a low value and the gas in the post-shock layer is compressed to a thin shell. The mean pressure in the hot bubble is several orders of magnitude higher than that of the ambient medium at this moment (Fig. 1 c), and drives the outward motion of the shell. This is called the pressure-driven snowplough (PDS) phase. An analytic model of a point-source explosion exhibits  $\eta = 2/7$  in the absence of radiative cooling in the hot bubble (McKee & Ostriker 1977). The power-law index of our results, however, deviates from that of the analytic model  $2/7$  because the interior pressure at the ST phase slightly increases the effective value of  $\eta$  (Cioffi et al. 1988; see Whalen et al. 2008, in detail). Note that the expansion law of the bubble will change with more realistic density distribution in the relic HII region, e.g., clumpiness, and radial density gradient. These effects should be separately examined in future studies. This phase continues as long as the mean interior pressure is much higher than the ambient pressure.

Radiative cooling is inefficient inside the bubble because of the extremely low density, and the gas loses thermal energy through adiabatic expansion instead. The mean interior pressure continues to decrease and becomes comparable to the ambient pressure at  $t = 4.6$  Myr. The motion of the shell is then driven by its momentum. This is a so-called momentum-conserving snowplough (MCS) phase. The thin shell model predicts that  $\eta = 1/4$ , but it is slightly higher in our results because of the contribution of finite pressure in the bubble (Cioffi et al. 1988). The shell's expansion velocity eventually falls to the sound speed of the ambient medium. In reality, the shell loses its identity thereafter and mixes with the ISM. This is the end of the lifetime of the shell.

The results of the other runs are similar to the fiducial one. In all cases, the SNRs enter the MCS phase before the end of the shell lifetime. This is because the ambient temperature monotonically decreases to a low value by radiative cooling. If the ambient matter is heated, for example, by external radiation, the MCS phase is unlikely to be reached.

#### 3.2 Thermal Evolution and Internal Structure of the Shell

Fig. 2 shows time evolution of the internal structure of the shell. Radial density and temperature profiles are presented against column density of hydrogen nuclei measured from the center. The column density of the shell increases as the shock front sweeps up the ambient materials, whereas the column density of the bubble decreases with time, because the mean density in the bubble quickly falls by the expansion. The mean density in the shell gradually decreases over the snowplough phase. This is because the shock strength becomes weaker and weaker as the bubble expands. The minimum temperature in the shell decreases with time. Note that it eventually falls below the CMB value. To see the physical processes, we plot in Fig. 3 the evolutionary trajectories of some typical fluid elements on the temperature-density diagram. These elements are taken into the shell in the snowplough phase. After they slightly drop from the initial location at  $(n_0, E_{\text{SN}}) = (1 \text{ cm}^{-3}, 10^4 \text{ K})$  by radiative cooling, the temperatures suddenly rise with the shock arrival. Due to fast cooling from atomic hydrogen, the post-shock layer cannot be resolved until the temperature falls back to  $\sim 10^4$  K, where the post-shock pressure balances with the ram pressure. However, our insufficient resolution there does not affect the evolution thereafter because the time-scale for the atomic cooling is very small compared with the entire evolutionary time-scale of the shell. For element (4) in Fig. 3, the radiative cooling rate and the chemical fractions are shown in Figures 4 and 5, respectively. Following the shock heating, the gas cools to somewhat below  $10^4$  K through the Ly  $\alpha$  emission. By this time, abundant  $\text{H}_2$  has formed as a result of a large amount of available electrons. The  $\text{H}_2$  abundance reaches as high as  $\sim 10^{-3}$  (Fig. 5), about an order of magnitude higher than that formed in an almost neutral gas. Below  $\simeq 8000$  K, the  $\text{H}_2$  becomes the most important coolant (Fig. 4). The  $\text{H}_2$  cooling reduces the temperature down to  $\sim 200$  K, giving rise to compression of the gas. The metal line cooling has a negligible effect during this phase because of the low abundance of metals (Fig. 4). Below  $\simeq 200$  K, the  $\text{H}_2$  cooling rate significantly drops and the other coolants cannot compensate for the inefficiency. At this moment, radiative cooling cannot reduce the shell pressure rapidly, while the ram pressure decreases faster than the shell pressure. As a result, the shell pressure becomes higher than the ram pressure and the shell begins to gradually distend to maintain the balance of pressure. This is seen in Fig. 3 as the turn-around of the trajectories at  $\sim 200$  K. The adiabatic expansion phase continues for  $\sim 10^6 - 10^7$  yr, which is much greater than a typical time-scale for the  $\text{H}_2$  cooling phase ( $\sim 10^5 - 10^6$  yr), until the shell dissolves into the ambient medium.

At low temperatures ( $\lesssim 150$  K), HD is known to form abundantly via the rightward reaction of



Although the temperature falls below the threshold for HD formation in our case, the density within the shell decreases as well. The reaction thus proceeds slower than the evolutionary time-scale of the shell, and the HD fraction is frozen to the final abundance of  $\sim 10^{-6}$ , which is an order of magnitude smaller than the total deuterium abundance (Fig. 5). The gradual density decrease causes the HD cooling to be inefficient. For  $T < T_{\text{CMB}}$ , the CMB heating via HD lines is weak and the trajectories in Fig. 3 exhibit the relation for the adiabatic expansion,  $T \propto n^{2/3}$ , except the highest density case of trajectory 1.

Note that the cooling time in the post-shock gas lengthens for smaller shock velocity, and reaches  $\sim 10^6$  yr for a gas entering the

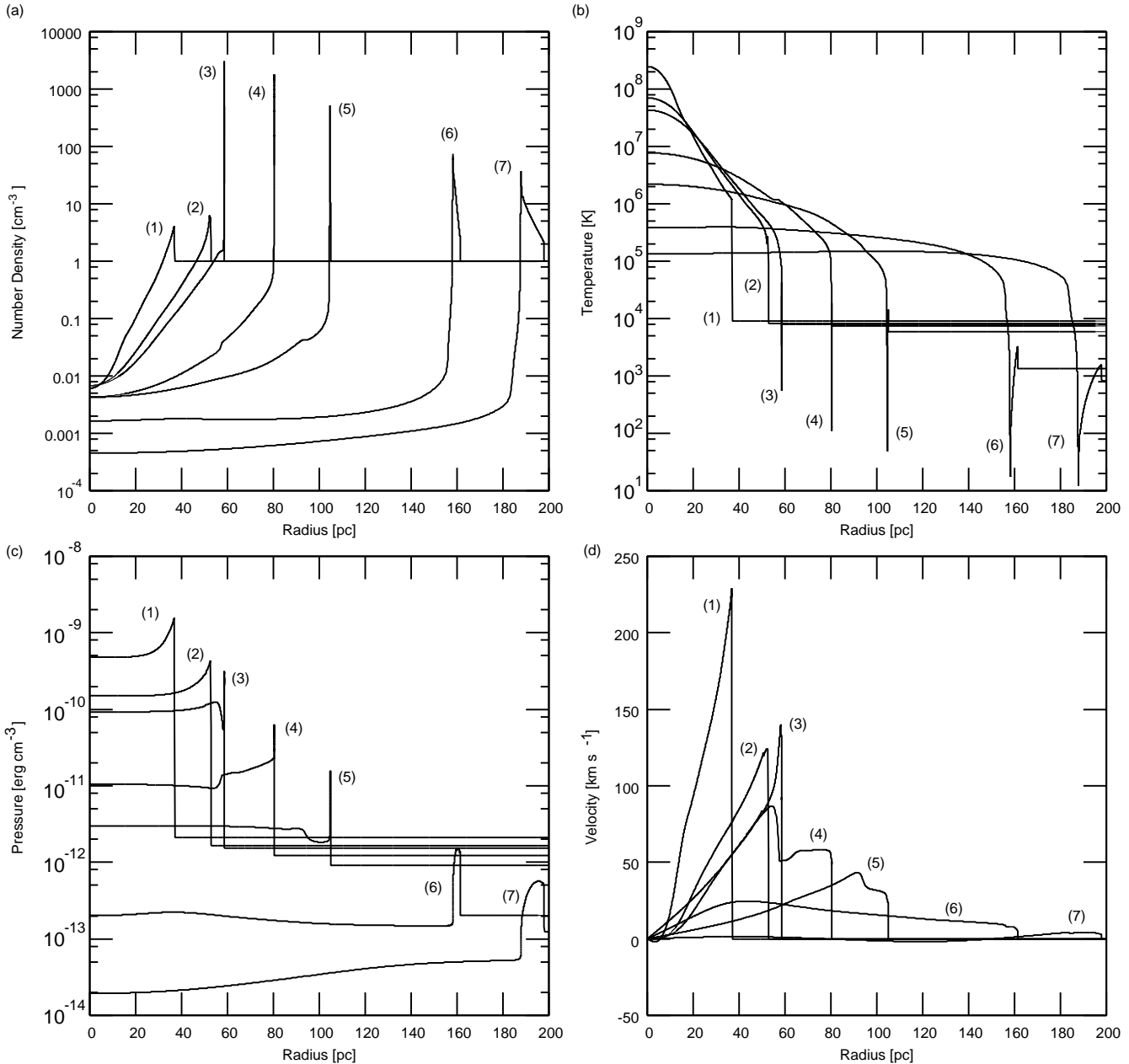


**Figure 1.** Evolution of radial distributions of (a) density, (b) temperature, (c) pressure, and (d) velocity for the fiducial run ( $E_{\text{SN}} = 10^{52}$  erg,  $n_0 = 1 \text{ cm}^{-3}$ ,  $Z = 10^{-4} Z_{\odot}$ ). Shown are the distributions at (1)  $9.0 \times 10^3$ , (2)  $4.8 \times 10^4$ , (3)  $1.7 \times 10^5$ , (4)  $4.9 \times 10^5$ , (5)  $1.1 \times 10^6$ , (6)  $5.0 \times 10^6$ , and (7)  $1.0 \times 10^7$  yr, respectively. The epochs (1) and (2) correspond to the Sedov-Taylor phase, and those from (3) to (7) to the snowplough phase.

shell during the MCS phase. Thus, the temperature at the outer edge of the shell remains high (Fig. 2 b). We use this result to explore the conditions for the shell fragmentation in Section 3.4.

### 3.3 Metallicity Effects on the Shell Evolution

For a high metallicity gas, metal cooling or heating becomes important at low temperatures ( $\lesssim 100$  K). In this section, we elaborate on this effect on the evolution of the shell. Fig. 6 shows the thermal evolution of some fluid elements for the parameters  $E_{\text{SN}} = 10^{52}$  ergs,  $n_0 = 1 \text{ cm}^{-3}$ , and  $Z = 10^{-2} Z_{\odot}$ , which is 100 times higher in metallicity than in the fiducial case. The trajec-

ories are almost the same as those in the fiducial run until they reach  $\sim 200$  K where the  $\text{H}_2$  cooling rate sharply decreases. In this case, the OI and then CI become the dominant coolants for  $< 300$  K and  $< 100$  K, respectively (Fig. 7). Unlike in the fiducial case, the temperatures approach the CMB value through radiative cooling rather than through the adiabatic expansion. With a rapid decrease in the radiative cooling rate near the CMB temperature, the shell begins to distend in a manner similar to the fiducial case. Owing to the metal cooling, the temperatures at which the shell starts to swell are lower than those in the fiducial case. When the temperature falls below the CMB value, the radiative heating via CI lines is effective enough to keep the temperature nearly constant at  $\sim 40$

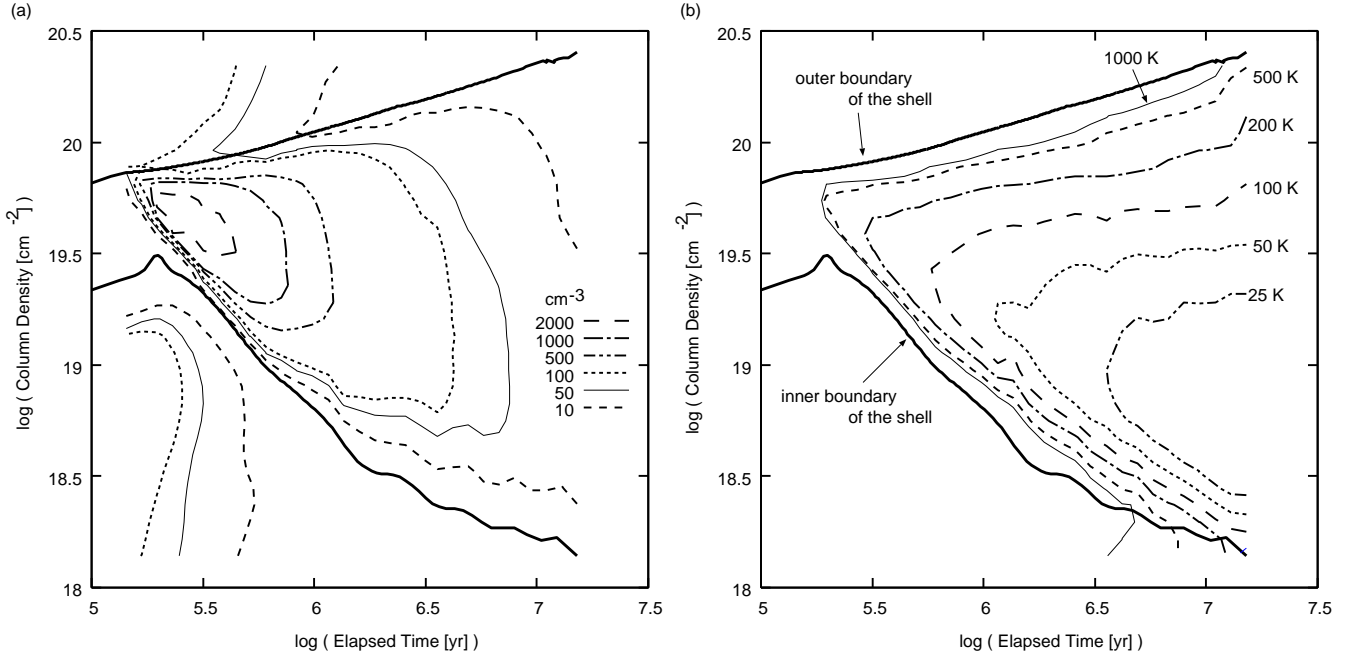


**Figure 2.** Contour maps for densities (a) and temperatures (b) in the shell as a function of time for the fiducial run ( $E_{\text{SN}} = 10^{52}$  erg,  $n_0 = 1 \text{ cm}^{-3}$ ,  $Z = 10^{-4} Z_{\odot}$ ). The longitudinal axis is the column density measured from the centre. The two thickest lines represent the boundaries of the shell. In figure (a), we show the iso-density surfaces of  $2000 \text{ cm}^{-3}$  (dashed),  $1000 \text{ cm}^{-3}$  (dotted-and-dashed),  $500 \text{ cm}^{-3}$  (double-dotted-and-dashed),  $100 \text{ cm}^{-3}$  (dotted),  $50 \text{ cm}^{-3}$  (solid), and  $10 \text{ cm}^{-3}$  (thick-dashed line). Figure (b) represents the iso-temperature surfaces of  $1000 \text{ K}$  (solid),  $500 \text{ K}$  (dashed),  $200 \text{ K}$  (dotted-and-dashed),  $100 \text{ K}$  (long-dashed),  $50 \text{ K}$  (dotted), and  $25 \text{ K}$  (double-dotted-and-dashed line).

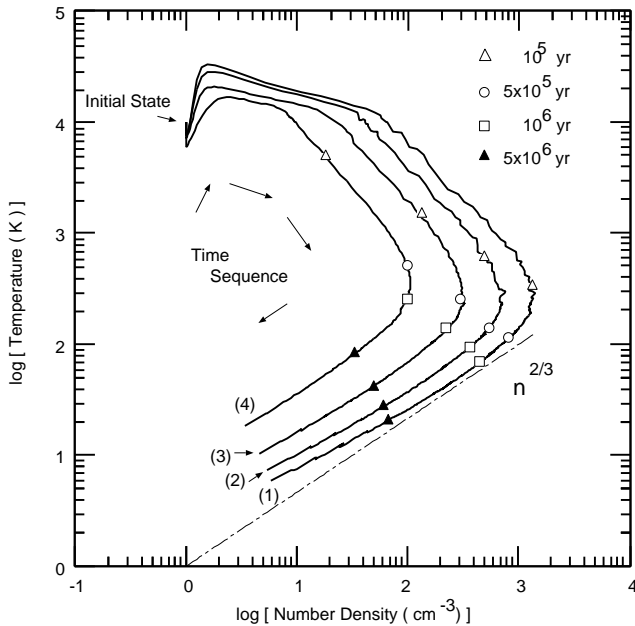


**Figure 3.** The evolution of four fluid elements on the density-temperature diagram in the fiducial run. The initial locations of the fluid elements are (1) 68, (2) 77, (3) 88, and (4) 104 pc from the centre. Those elements enter the shell in the snowplough phase. The arrows indicate the direction of evolution. The circles, triangles, squares and black triangles are indicate the times  $10^5$  yr,  $5 \times 10^5$  yr,  $10^6$  yr and  $5 \times 10^6$  yr, respectively, after which the shock-compressed gas cools to  $10^4$  K.

K, although with a gradual decrease in the temperatures. Thus, the final temperatures are somewhat higher than in the fiducial case.

How much metallicity is needed to affect the evolution of the shell? To answer this question, we performed other simulations with metallicity  $Z = 10^{-3} Z_{\odot}$ , and found that the metal cooling remains below that of HD molecules. Hence, in this case, the evolution of the shell is almost the same as in the fiducial case. We conclude that the minimum metallicity necessary to affect the thermal evolution of the shell is  $\sim 10^{-2} Z_{\odot}$ . We will mention its influence on the conditions for the shell fragmentation in Section 3.4.

### 3.4 Fragmentation of the Shell

#### 3.4.1 Overview of Linear Perturbation Analyses

Here, we discuss whether the supernova-driven shell fragments into pieces before it dissolves into the ambient medium. When the shell fragments by gravitational instability, the next-generation stars are expected to form from the fragments. Conditions for fragmentation of an expanding and decelerating shell have been studied by several authors both analytically (Vishniac 1983; Nishi 1992; Elmegreen 1994; Whitworth et al. 1994) and numerically (Yoshida & Habe 1992; Mac Low & Norman 1993). The linear analysis by Elmegreen (1994) showed that the instantaneous growth rate of density perturbations for transverse motion at wavenumber  $k$  is given by

$$\omega(k, t) = -3\frac{V}{R} + \sqrt{\frac{V^2}{R^2} - k^2 c_s^2 + 2\pi G \Sigma_0 k}, \quad (7)$$

where  $R$ ,  $V$ ,  $\Sigma_0$ , and  $c_s$  are the radius, velocity, unperturbed column density, and sound speed of the shell, respectively. Here, the perturbations are assumed to grow in a way similar to  $\exp(\omega t)$ . The

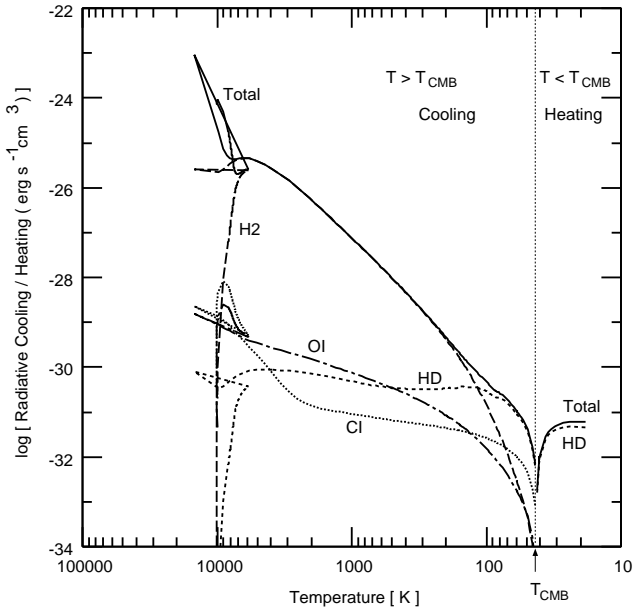


**Figure 4.** Radiative cooling and heating rate of a typical fluid element (4 in Figure 3) against the temperature. The vertical dotted line shows the CMB temperature,  $T_{\text{CMB}} = 44$  K, below which the processes work as heating. The lines represent the radiative rates of  $\text{H}_2$  (long-dashed), HD (dashed), CI (dotted) and OI (dotted-and-dashed). The solid line shows the total rate, including the H atomic cooling.

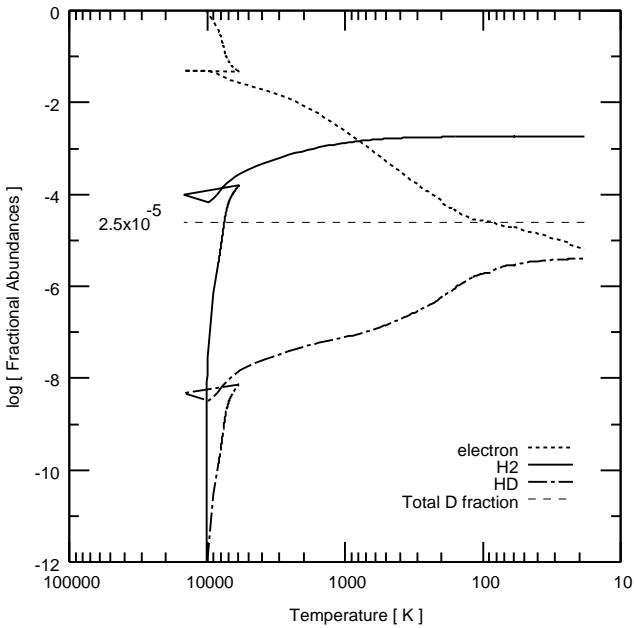


**Figure 5.** Evolution of the  $\text{H}_2$  (solid), HD (dotted-and-dashed) and electron (dotted) fractions at the same fluid element as Figure 4 against the temperature. The horizontal dashed-line represents the total deuterium abundance of  $2.5 \times 10^{-5}$ . The effect of the shock is observed as the kinks in the fraction curves. Thereafter the temperature continues to decrease, while the  $\text{H}_2$ , and HD fractions gradually increase.

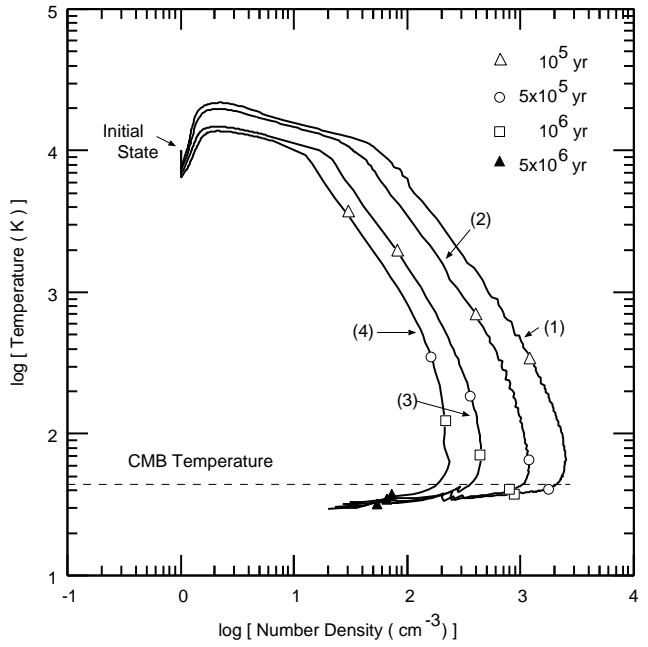


**Figure 6.** Same as Fig. 3, except for the metallicity  $Z = 10^{-2} Z_{\odot}$ . The horizontal dashed-line represents the CMB temperature at  $z = 15$ .

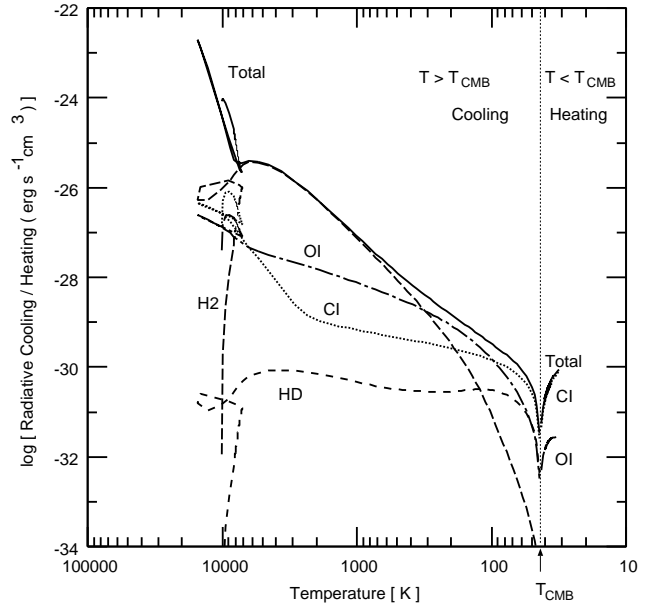


**Figure 7.** Same as Fig. 4, but for the fluid element (4) in Figure 6, with metallicity  $10^{-2} Z_{\odot}$ .

seeds of density perturbations are generated, for instance, by the decelerating shock instability (Mac Low & Norman 1993), or by the shock propagation into the inhomogeneous medium. The perturbations grow by collecting the ambient medium, while the new mass accretion onto the shell increases total transverse momentum. In addition, the spherical expansion stretches and attenuates perturbations. These processes are taken into account via the  $V/R$  terms in equation (7) and the net effect acts to hinder growth of the per-

turbations. The maximum growth rate,

$$\omega_{\max} = -3\frac{V}{R} + \sqrt{\left(\frac{V}{R}\right)^2 + \left(\frac{\pi G \Sigma_0}{c_s}\right)^2}, \quad (8)$$

is attained at wavenumber

$$k_{\max} = \frac{\pi G \Sigma_0}{c_s^2}. \quad (9)$$

The shell becomes gravitationally unstable if  $\omega_{\max} > 0$ , i.e.,

$$t_{\text{exp}} \equiv \frac{R}{V} > \frac{8^{1/2} c_s}{\pi G \Sigma_0} \sim \frac{t_{\text{ff}}^2}{t_{\text{cross}}}, \quad (10)$$

where  $t_{\text{exp}}$ ,  $t_{\text{ff}}$ , and  $t_{\text{cross}}$  are the shell expansion time, free-fall time in the shell, and the sound crossing time for the shell width, respectively.

Even when the shell becomes gravitationally unstable, it takes some time for the perturbations to grow to induce the fragmentation. The time-scale for fragmentation can be roughly estimated by  $1/\omega_{\max}$ . It should be noted, however, that the growth rate for a fixed wavenumber changes with time because  $V/R$  and  $\Sigma_0$  in equation (7) are modified by the mass accretion. To evaluate the typical fragmentation scale, we keep track of all the modes that attain the maximum growth rate during the shell history. For those modes, we define the fragmentation time  $t_f$  as:

$$\int_{t_i}^{t_f} \omega(k, t) dt = 1, \quad (11)$$

where  $t_i$  is the time when the mode  $k$  first becomes unstable. Namely,  $t_f$  is the time for the perturbation to grow  $e$  times the initial value. When condition (11) is met, the shell is assumed to fragment into pieces with scales corresponding to  $k_{\max}$  (Ehlerová et al. 1997; Elmegreen, Palouš & Ehlerová 2002). We evaluate the fragment mass by

$$M_{\text{frag}}(\lambda_{\max}, t_f) = \pi \left(\frac{\lambda_{\max}}{2}\right)^2 \Sigma_0(t_f), \quad (12)$$

where  $\lambda_{\max} \equiv 2\pi/k_{\max}$ .

The shell loses its identity when it slows down to the sound speed of the ambient medium. For triggering subsequent star formation, fragmentation must occur within the lifetime of the shell.

### 3.4.2 Application of the Linear Analysis

In this section, we use the result of the linear analysis to find the conditions for fragmentation of a supernova-driven shell. The dispersion relation (8) is derived with one-zone approximation to the shell, whereas the shell has a stratified structure in our simulations. The application of the linear analysis to our result is, therefore, not straightforward. If the stratified structure is maintained until the shell disappears, the gravitational instability seems to occur first in a cold layer of the shell due to its low temperature. However, this is not the case because the mass of the cooled gas is not sufficient to trigger the gravitational instability. On the contrary, the coldest layer tends to gradually expand as discussed in Section 3.2, indicating that the self-gravity is not important there. In reality, the gravitational instability most easily occurs at the scale comparable to the width of the shell because the column density of the layer must be high enough for fragmentation. We then simply estimate a representative temperature by taking mass-weighted average over the whole shell.

In Fig. 8, we show the parameter range of  $(E_{\text{SN}}, n_0)$  where the shell fragments within its lifetime for runs with  $Z = 10^{-4} Z_{\odot}$

and  $10^{-2} Z_{\odot}$ . Metallicity affects the result only for  $(E_{\text{SN}}, n_0) = (10^{52}, 10)$ , where the  $10^{-4} Z_{\odot}$  run satisfies condition (10) but not (11) before the dissolution of the shell. For high ambient density, the shell accumulates a large amount of gas within the lifetime and fragments even in the case of  $10^{-4} Z_{\odot}$ . Thus, the metallicity dependence disappears for such high ambient densities. In the cases of  $E_{\text{SN}} = 10^{52}$  erg, the shell fragmentation occurs for both metallicities at the ambient density  $\geq 10^2 \text{ cm}^{-3}$ . For lower explosion energy  $E_{\text{SN}} = 10^{51}$  erg, this threshold density increases to  $10^3 \text{ cm}^{-3}$ . In Fig. 8, we also plot the conditions for shell fragmentation found by Salvaterra et al. (2004) and Machida et al. (2005) for comparison. The discrepancy among their conditions stems from the difference in their adopted shell temperatures and criteria for fragmentation. Our result almost coincides with that by Salvaterra et al. (2004) because their assumed temperature is almost the same as ours. As long as the mean temperature falls to 200 – 300 K through  $\text{H}_2$  cooling, the total amount of gas swept up into the shell does matter for fragmentation. Thus, the conditions for fragmentation rely heavily on the ambient density as well as explosion energy, but little on the metallicity.

In Table 1, we show the properties of the shell at fragmentation time  $t_f$ . There is a range of the fragment mass because some unstable modes fulfill the condition (11) soon after  $t_f$ . This means that the fragmentation scale depends largely on the shape of initial perturbation, or that the shell fragments with a wide range of mass scales. The fragment mass for models with  $n_0 \geq 10^2 \text{ cm}^{-3}$  is in the range  $10^2 - 10^3 M_{\odot}$ , while that for a model with  $n_0 = 10 \text{ cm}^{-3}$  is an order of magnitude lower. Because the wavelength  $\lambda_{\max}$  lengthens for the smaller column density (see equation 9), the fragment mass becomes higher for lower ambient density.

## 4 DISCUSSIONS

### 4.1 Significance of Star Formation Triggered by Supernova Explosions

The supernova explosion is an important feedback process influencing cosmic star formation history as well as the nearby star formation activity. We have shown that supernova explosions induce subsequent star formation as a result of shell fragmentation in a high-density environment (see Fig. 8). Here, we estimate the critical mass of haloes above which second-generation stars form in the induced manner, using our results. We assume that the explosion occurs at the centre of the halo. We have derived the minimum ambient density  $\rho_{\text{min}}$  for a given explosion energy, at which the shell fragments at a radius  $r_f$ . Thus, the condition for the shell fragmentation is that the column density exceeds  $\rho_{\text{min}} r_f / 3$  at a radius  $< r_f$ , or in other words, the mean density  $\bar{\rho}_f$  within the radius  $r_f$  is lower than  $\rho_{\text{min}}$ . We evaluate the mean density  $\bar{\rho}_f$  assuming the density profile in the halo  $\rho(r) \propto r^{-w}$ , with the index  $w \simeq 2$  as suggested by numerical calculations of the first star formation.

Using the mean density  $\bar{\rho}_{\text{vir}}(z_c)$  and virial radius  $r_{\text{vir}}$  of a halo virializing at  $z_c$ , we obtain the mean baryonic density inside  $r_f$  as

$$\bar{\rho}_f = \frac{\Omega_b}{\Omega_m} \bar{\rho}_{\text{vir}}(z_c) \left(\frac{r_f}{r_{\text{vir}}}\right)^{-2} \quad (13)$$

$$\simeq 3.0 \times 10^{-25} \text{ g cm}^{-3} \left(\frac{1+z_c}{16}\right)^3 \left(\frac{r_f}{r_{\text{vir}}}\right)^{-2}. \quad (14)$$

Here, we apply the spherical collapse model to the mean density in the halo,  $\bar{\rho}_{\text{vir}} = 18\pi^2 (\Omega_b / \Omega_m) \rho_b(z_c)$ , where  $\rho_b$  is the background density (e.g., Padmanabhan 1993). By eliminating  $r_{\text{vir}}$  in equation



$(E_{\text{SN}}, n_0, Z)$ (erg, $\text{cm}^{-3}$ , $Z_{\odot}$ )	$T_{\text{sh}}$ (K)	$\Sigma_0$ ( $\text{g}/\text{cm}^{-2}$ )	$\Delta R$ (pc)	$\bar{\rho}_{\text{sh}}$ ( $\text{g}/\text{cm}^{-3}$ )	$t_{\text{max}}$ (Myr)	$t_f$ (Myr)	$\lambda_{\text{max}}$ (pc)	$R_{\text{sh}}$ (pc)	$M_{\text{sh}}$ ( $M_{\odot}$ )	$M_{\text{frag}}$ ( $M_{\odot}$ )	$M_{\text{frag}}^{\text{min}}$ ( $M_{\odot}$ )	$M_{\text{frag}}^{\text{max}}$ ( $M_{\odot}$ )	$M_{\text{crit}}$ ( $M_{\odot}$ )
$(10^{51}, 10^3, 10^{-4})$	46	$2.2 \times 10^{-2}$	0.78	$9.2 \times 10^{-21}$	1.0	1.7	3.6	9.9	$1.3 \times 10^5$	$1.1 \times 10^3$	$2.8 \times 10^2$	$2.7 \times 10^3$	$6.6 \times 10^7$
$(10^{51}, 10^3, 10^{-2})$	45	$2.3 \times 10^{-2}$	0.74	$1.0 \times 10^{-20}$	0.53	1.6	3.1	10	$1.3 \times 10^5$	$8.1 \times 10^2$	$2.4 \times 10^2$	$8.5 \times 10^2$	$6.7 \times 10^7$
$(10^{52}, 10^3, 10^{-4})$	83	$3.7 \times 10^{-2}$	0.54	$2.3 \times 10^{-20}$	0.84	1.4	2.6	17	$6.6 \times 10^5$	$9.5 \times 10^2$	$5.9 \times 10^2$	$2.2 \times 10^3$	$3.3 \times 10^8$
$(10^{52}, 10^3, 10^{-2})$	46	$3.7 \times 10^{-2}$	0.49	$2.4 \times 10^{-20}$	0.35	1.5	2.0	16	$5.5 \times 10^5$	$5.8 \times 10^2$	$1.4 \times 10^2$	$6.1 \times 10^2$	$2.7 \times 10^8$
$(10^{52}, 10^2, 10^{-4})$	75	$9.8 \times 10^{-3}$	2.1	$1.6 \times 10^{-21}$	3.0	4.5	9.3	43	$1.1 \times 10^6$	$3.2 \times 10^3$	$2.3 \times 10^2$	$5.8 \times 10^3$	$1.8 \times 10^8$
$(10^{52}, 10^2, 10^{-2})$	51	$9.4 \times 10^{-3}$	1.6	$1.9 \times 10^{-21}$	2.4	4.0	7.0	41	$9.7 \times 10^5$	$1.7 \times 10^3$	$3.9 \times 10^2$	$2.3 \times 10^3$	$1.5 \times 10^8$
$(10^{52}, 10, 10^{-2})$	55	$2.5 \times 10^{-3}$	7.4	$1.2 \times 10^{-22}$	9.3	15	29	110	$1.9 \times 10^6$	$8.0 \times 10^3$	$4.4 \times 10^3$	$2.0 \times 10^4$	$9.6 \times 10^7$
$(10^{53}, 10^3, 10^{-4})$	87	$5.5 \times 10^{-2}$	0.16	$1.1 \times 10^{-19}$	0.33	0.88	2.3	24	$1.9 \times 10^6$	$1.1 \times 10^3$	$1.9 \times 10^2$	$1.5 \times 10^3$	$9.2 \times 10^8$
$(10^{53}, 10^2, 10^{-4})$	78	$1.5 \times 10^{-2}$	0.61	$7.8 \times 10^{-20}$	2.2	3.0	5.7	65	$3.7 \times 10^6$	$1.8 \times 10^3$	$6.1 \times 10^2$	$3.3 \times 10^3$	$5.8 \times 10^8$
$(10^{53}, 10, 10^{-4})$	105	$4.1 \times 10^{-2}$	3.7	$3.6 \times 10^{-22}$	6.9	11	26	180	$7.9 \times 10^6$	$9.9 \times 10^3$	$8.5 \times 10^3$	$1.5 \times 10^4$	$1.8 \times 10^7$

**Table 1.** Properties of the shell when the shell fragmentation first occurs. The left column is the model parameters. The notation  $T_{\text{sh}}$  represents the mass-weighted mean temperature in the shell,  $\Sigma_0$  the column density,  $\Delta R$  the width of the shell,  $\bar{\rho}_{\text{sh}}$  the mean density in the shell,  $t_{\text{max}}$  the time when the shell becomes gravitationally unstable first,  $t_f$  the fragmentation time,  $\lambda_{\text{max}}$  the wavelength of perturbation which becomes unstable first,  $R_{\text{sh}}$  and  $M_{\text{sh}}$  the radius and mass of the shell at fragmentation, and  $M_{\text{frag}}$  the mass of the fragments,  $M_{\text{frag}}^{\text{min}}$  the minimum mass of the fragments after  $t_f$ ,  $M_{\text{frag}}^{\text{max}}$  the maximum mass of the fragments after  $t_f$ . The last column is the critical halo mass below which star formation cannot occur in the induced manner.

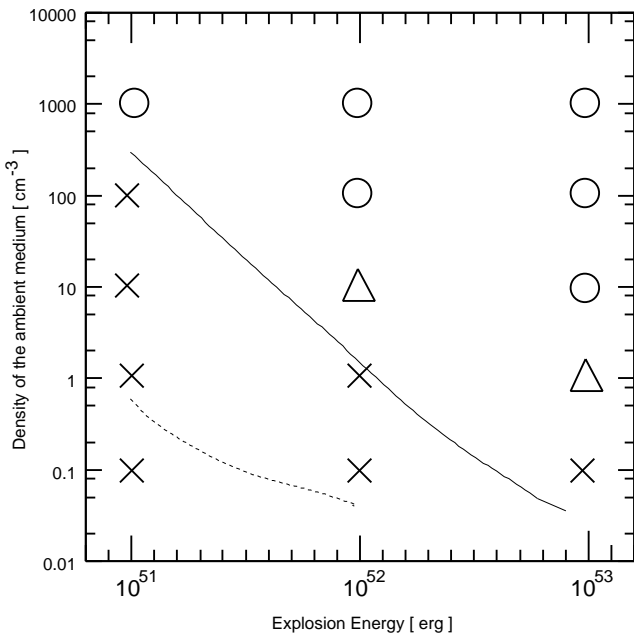


**Figure 8.** Dependence of the fragmentation result of the shell on the ambient density and explosion energy for metallicities  $Z = 10^{-2}Z_{\odot}$  and  $Z = 10^{-4}Z_{\odot}$ . In the cases of  $E_{\text{SN}} = 10^{51}$  and  $10^{52}$  erg, the circles, triangle, and crosses mean that the fragmentation occurs for both metallicities, only for  $Z = 10^{-2}Z_{\odot}$ , and for neither, respectively. In the cases of  $E_{\text{SN}} = 10^{53}$  erg, the circles and crosses represent the successes and fails of the fragmentation respectively, and the triangle satisfies the condition (10) but does not equation (11). Also plotted are the results by Salvaterra et al. (2004; solid) and Machida et al. (2005; dotted), above which the fragmentation occurs.

(13) with  $M_{\text{halo}} = (4\pi/3)\bar{\rho}_{\text{vir}}r_{\text{vir}}^3$ , the halo mass  $M_{\text{halo}}$  can be expressed as

$$M_{\text{halo}} = \frac{4\pi}{3}\bar{\rho}_{\text{vir}}^{-1/2}(z_c)r_f^3\left(\frac{\Omega_b}{\Omega_m}\right)^{-3/2}\bar{\rho}_f^{3/2}. \quad (15)$$

Setting  $\bar{\rho}_f = \rho_{\text{min}}$ , we obtain the critical halo mass for triggered

star formation:

$$M_{\text{halo}}^{\text{crit}} \simeq 1.5 \times 10^8 M_{\odot} \left(\frac{1+z_c}{16}\right)^{-1.5} \left(\frac{r_f}{41.4 \text{pc}}\right)^3 \left(\frac{n_{\text{min}}}{10^2 \text{cm}^{-3}}\right)^{1.5}, \quad (16)$$

where  $n_{\text{min}} = \rho_{\text{min}}/\mu m_{\text{H}}$ . Note that the dependence on ambient density  $n_{\text{min}}$  is also included through the fragmentation radius  $r_f$ . The critical halo masses range from  $1.8 \times 10^7 M_{\odot}$  to  $9.2 \times 10^8 M_{\odot}$ . These values are listed in Table 1. These mass-scales correspond to  $\approx 3\sigma$  fluctuations virializing at  $z = 15$  and the abundance of such objects is about a few per cubic Mpc. The critical mass for triggered star formation  $M_{\text{halo}}^{\text{crit}}$  exceeds the halo mass of  $4.7 \times 10^7 M_{\odot} [(1+z_c)/16]^{-3/2}$  corresponding to the virial temperature of  $10^4$  K (Barkana & Loeb 2001), and consequently, star formation triggered by a supernova explosion is unlikely to occur in low-mass haloes ( $T_{\text{vir}} < 10^4$  K) where primordial stars form solely via  $\text{H}_2$  cooling. Instead, in such low-mass haloes, the expanding SNR evacuates all the gas and quenches the subsequent star formation activity. The triggering process becomes increasingly important at lower redshift as more massive haloes of  $> 10^{8-9} M_{\odot}$  begin to form.

So far, we have assumed the density distribution  $\rho \propto r^{-2}$ , which is appropriate at the stellar birth. If an expanding HII region created during the stellar lifetime disturbs and even blows the surrounding material away from the host halo before the supernova explosion, the column density of the supernova-driven shell is significantly reduced and the subsequent triggering process does not work. This effect is important in low-mass ( $\lesssim 10^6 M_{\odot}$ ) haloes (Kitayama & Yoshida 2005; Whalen et al. 2008). However, in massive haloes ( $\gtrsim 10^8 M_{\odot}$ ) where the triggered process is possible, the HII region is trapped deep inside the virial radius and barely removes any gas from the host haloes. Thus, the expansion of the HII region does not change our criteria for the triggered star formation. Here, it should be noted that the densities in the centre of the trapped HII regions are  $10^4 - 10^7 \text{cm}^{-3}$  and much higher than we have examined, according to some numerical simulations (Kitayama & Yoshida 2005; Whalen et al. 2008). The reason why we have investigated the density range of  $10^2 - 10^3 \text{cm}^{-3}$  is only for comparison with the previous works of Salvaterra et al. (2004) and Machida et al. (2005).

Whalen et al. (2008) studied supernova explosions in neutral haloes undisturbed by the expansion of HII regions. They showed that the SNR is trapped by the deep gravitational potential well

of the dark matter. It initially expands out to  $\sim 50$  pc, and then turns to fall back. Metals in the ejecta will mix with gas in the halo before the SNR stagnates. The polluted gas may fragment into clumps through metal fine-structure line cooling, which leads to subsequent star formation. This triggering mode is beyond the scope of this paper, and to be examined in future studies. In addition, we have ignored another process of possibly triggering star formation described below because of a limitation of our simulations. The HII region prior to the supernova sweeps up materials into a shell (Kitayama et al. 2004; Whalen et al. 2004). The SNR catches up with the pre-existing shell. Whalen et al. (2008) showed that the collision is quite violent and would mix heavy elements from the ejecta with materials in the shell. Fracturing the ejecta into the dense shell and the resultant enhanced cooling could lead to star formation. The shell/ejecta interaction occurs even in low-mass halos of  $\lesssim 10^8 M_\odot$ . Thus, simulations with more realistic density distribution are needed for a complete survey of the conditions required for triggered star formation.

We finally note that hydrodynamical mixing of metals in the SNR is generally important for realistic evolution. Even if the ambient medium is constituted by pristine H and He gas, the polluted gas will cool via metal fine-structure lines. Although our calculations with pre-enriched ambient medium predict that the critical halo mass needed for triggering star formation depends hardly on metallicity, it is still uncertain how the hydrodynamical mixing spreads metals into the SNR and affects the triggering processes.

## 4.2 Subsequent Evolution of the Fragments and Possibility of Low-mass Star Formation

After the fragmentation, each fragment continues to contract through its own gravity. Although the mass of fragments is  $\sim 10^3 - 10^4 M_\odot$  (Table 1), they are expected to fragment once again into smaller ( $< 10 M_\odot$ ) pieces. The shell initially fragments into disk-like clouds, and then further fragmentation leads to smaller filamentary clouds (Miyama, Narita & Hayashi 1987). Nakamura & Umemura (2001, 2002) examined fragmentation of primordial filamentary clouds and concluded that they fragment into spherical cores of  $1 - 10^2 M_\odot$ , the exact value of which depends on the initial cloud density  $n_c$  and gravity-to-pressure ratio  $f$ . The fragmentation leads to low-mass ( $\sim 1 M_\odot$ ) cores only if the conditions that  $n_c \gtrsim 10^5 \text{ cm}^{-3}$  and  $f > 3$  are met. Salvaterra et al. (2004) pointed out that these conditions are easily satisfied and thus low-mass star formation occurs in the supernova-driven shell in primordial environments. However, our more detailed calculations demonstrated that the number density in the shell never exceeds  $10^5 \text{ cm}^{-3}$  for the ambient density  $n_0 \leq 10^3 \text{ cm}^{-3}$ , and the low-mass stars are unlikely to form without any metal enrichment even in the triggered fashion.

Provided that the metallicity is higher than  $Z_{\text{crit}} = 10^{-5} - 10^{-6} Z_\odot$  and a sizeable portion  $\sim 0.5 - 1$  of those metals condenses into dust grains, fragmentation is induced by dust cooling at high densities  $> 10^{10} \text{ cm}^{-3}$  (Schneider et al. 2002, 2006; Omukai et al. 2005; Tsuribe & Omukai 2006, 2008; Clark, Glover & Klessen 2008). In the early universe, dust grains originate from supernovae (Todini & Ferrara 2002; Nozawa et al. 2003; Schneider, Ferrara & Salvaterra 2004) rather than the AGB stars. Nozawa et al. (2007) studied the formation of dust grains in population III supernovae and their destruction by the reverse shock. They concluded that the mass of the surviving dust grains in the shell is at most  $0.1 M_\odot$  for the ambient density  $n_0 = 10 \text{ cm}^{-3}$  at  $t \sim 0.7$  Myr. To reach the critical metallicity  $Z_{\text{cr}}$ , the total mass in the shell should be less

than  $5 \times 10^6 (Z_{\text{cr}}/10^{-6} Z_\odot)^{-1} M_\odot$  before fragmentation, under the assumption of homogeneous grain distribution within the shell. Because the shell mass at fragmentation is  $\sim 10^6 M_\odot$  for  $n_0 = 10 \text{ cm}^{-3}$  (Sec.3), low-mass stars can be triggered by the first supernova.

## 4.3 Effects of External Photo-dissociating Radiation

We assume that  $\text{H}_2$  molecules in the ambient medium are completely photo-dissociated by the central star before the supernova, but they are replenished quickly due to a high fraction of the catalyst electrons in our calculations. As a result, the ambient temperature decreases to several hundreds of Kelvins owing to the  $\text{H}_2$  cooling (Fig. 1). However, we have not considered the effects of any external radiation. Once stars appear in the universe, they build up a background of  $\text{H}_2$  dissociating radiation, which delays subsequent star formation (e.g., Haiman, Rees & Loeb 1997; Haiman, Abel & Rees 2000). If an external radiation flux dissociates the  $\text{H}_2$  molecules, the gas temperature remains higher because of inefficient cooling. The low temperature in the ambient medium prolongs the lifetime of the shell. The fragmentation time is slightly shorter than the shell lifetime even in our calculation, and thus the fragmentation may not occur with external heating.

According to a cosmological simulation by Johnson, Greif & Bromm (2008), the photo-dissociating radiation flux is  $J_{21} \lesssim 0.04$  at 12.87 eV in units of  $10^{-21} \text{ erg s}^{-1} \text{ cm}^{-2} \text{ Hz}^{-1} \text{ sr}^{-1}$ . For this background, the  $\text{H}_2$  dissociation timescale is  $t_{\text{diss}} \approx 6 \times 10^5 (J_{21}/0.04)^{-1} \text{ yr}$  (Abel et al. 1997), whereas the typical  $\text{H}_2$  formation time behind the shock in our calculation is  $t_{\text{form}} \sim 10^4 \text{ yr}$  at the beginning of the PDS phase. The formation time is thus an order of magnitude shorter than the dissociation time. Hence, the external photo-dissociating flux does not prevent the  $\text{H}_2$  formation at this phase. Soon after that, the  $\text{H}_2$  column density of the shell rapidly increases to shield the photo-dissociation (i.e.,  $\gtrsim 10^{14} \text{ cm}^{-2}$ ; e.g., Draine & Bertoldi 1996) as seen below. Before the photo-dissociation, the  $\text{H}_2$  column density of the shell reaches  $\sim y(\text{H}_2) n_{\text{H}} v_{\text{sh}} t_{\text{diss}}$ , where  $y(\text{H}_2)$  and  $v_{\text{sh}}$  are the fractional abundance of  $\text{H}_2$  molecules and shock velocity. The shock velocity is on the order of  $10^2 \text{ km s}^{-1}$  at the incipient PDS phase, while  $n_{\text{H}}$  is enhanced to  $\sim \mathcal{M}^2 n_0$  by an isothermal shock with the Mach number  $\mathcal{M}$ . The  $\text{H}_2$  fract ion necessary for self-shielding is then only

$$y_{\text{H}_2} \sim 10^{-8} \left( \frac{v_{\text{sh}}}{10^2 \text{ km/s}} \right)^{-1} \left( \frac{t_{\text{diss}}}{10^6 \text{ yr}} \right)^{-1} \left( \frac{n_0}{1 \text{ cm}^{-3}} \right)^{-1}, \quad (17)$$

where we assume that  $\mathcal{M} \sim 10$ . Because the  $\text{H}_2$  abundance far exceeds this value within the dissociation time (Fig. 5), we conclude that the external photo-dissociating radiation does not significantly prevent  $\text{H}_2$  formation in the shell.

## 4.4 Effects of Non-gravitational Instabilities

In our analysis of gravitational instability, we have implicitly assumed that the coherence of the layer is not destroyed by some dynamical instabilities emerging before the gravitational one. For instance, the decelerating shock instability is expected to grow from the linear analysis (Vishniac 1983). Mac Low & Norman (1993) numerically demonstrated, however, that this instability saturates at a rather low amplitude in the non-linear stage, and does not significantly disturb the shell structure. The thermal instability is also expected to occur in the rapid cooling phase in the shocked layer.

Koyama & Inutsuka (2002) studied propagation of a shock into the contemporary ISM and fragmentation of a shock-compressed layer, taking account of cooling, heating, and thermal conduction. They showed that the thermal instability causes the cooled layer to fragment into small ( $\sim 10 - 100$  AU) cloudlets with some translational motions. Bromm, Yoshida & Hernquist (2003) simulated the first supernova explosions, and showed that the swept-up shell consists of small cloudlets, which are presumably formed by thermal instability. The motions of the cloudlets effectively enhance the sound speed within the shell, leading to delay in growth of the gravitational instability. After the shell fragments through the gravitational instability, the cloudlets will aggregate into a larger cloud with the contraction of the fragments. This may ultimately lead to cluster star formation (Elmegreen 1998). Thus, thermal instability influences not only the shell fragmentation but also the subsequent star formation in the fragments. Although our one-dimensional calculations cannot clarify the detailed fragmentation processes in the shell and subsequent evolution of the fragments, future multi-dimensional simulations are expected to reveal them.

## 5 SUMMARY

To explore the possibility of star formation triggered by supernovae in the early universe, we have studied the evolution of shells formed around the supernova bubble during the snowplough phase in low-metallicity environments. We investigated detailed structure of the shell, using spherical symmetric hydrodynamics with non-equilibrium chemistry for different sets of ambient densities, explosion energies, and metallicities. Our results are summarized as follows:

(i) We have demarcated the ranges of metallicity in terms of thermal evolution of the shell:

- For metallicities with  $< 10^{-2} Z_{\odot}$ , the post-shock gas first cools promptly to  $\sim 200$  K through the  $H_2$  cooling, and then progressively to a lower value through adiabatic expansion. Although 10 % of the deuterium transforms into HD in the shell, the HD cooling and heating have never become important because of decreasing density.

- For higher metallicities ( $> 10^{-2} Z_{\odot}$ ), the fine-structure line transitions of O and C reduce the post-shock gas below 100 K. After the radiative cooling becomes inefficient, the gas then adiabatically expands as in the lower-metallicity cases. The CMB heating via the C I fine-structure transitions hinders the gas from cooling below the CMB temperature.

(ii) We have examined whether the swept-up shell becomes gravitationally unstable before it mixes with the ISM, using the linear perturbation analysis. Fragmentation of the shell easily occurs in denser ISM and for higher explosion energies because these conditions are favourable to attaining the column density of the shell necessary for fragmentation. The criteria for the fragmentation depend little on metallicity as thermal evolution of the shell is not so sensitive to it.

(iii) We have evaluated the fragment mass from the wavelength of the maximum growth modes. Because the wavelength is inversely proportional to the column density, the fragment mass becomes lower for both higher ambient densities and higher explosion energies. The resulting fragment mass is  $10^2 - 10^3 M_{\odot}$ .

(iv) We have derived the critical halo mass  $M_{\text{halo}}^{\text{crit}} \simeq 10^8 M_{\odot}$  above which star formation can be triggered by a supernova explo-

sion. In minihaloes ( $< 10^6 M_{\odot}$ ) where the first stars are more likely to form, this triggering mechanism does not work.

## ACKNOWLEDGMENTS

We thank M. N. Machida, M. Nagashima, and S. Inutsuka for helpful comments and discussions. This study is supported in part by Research Fellowships of the Japan Society for the Promotion of Science for Young Scientists (T. N. and T. H.).

## REFERENCES

- Abel T., Anninos P., Zhang Y., Norman M. L., 1997, *New Astron.*, 2, 181  
 Abel T., Bryan G. L., Norman M. L., 2002, *Sci*, 295, 93  
 Anders E., Grevesse N., 1989, *GeCoA*, 53, 197  
 Barkana R., Loeb A., 2001, *Phys. Rep.*, 349, 125  
 Bianchi S., Schneider R., 2007, *MNRAS*, 378, 973  
 Bromm V., Coppi P. S., Larson R. B., 2002, *ApJ*, 564, 23  
 Bromm V., Yoshida N., Hernquist L., 2003, *ApJ*, 596, L135  
 Cen R., 1992, *ApJS*, 78, 341  
 Cen R., Riquelme M. A., 2008, *ApJ*, 674, 644  
 Chevalier R. A., 1974, *ApJ*, 188, 501  
 Cioffi D. F., McKee C. F., Bertschinger E., 1988, *ApJ*, 344, 252  
 Clark P. C., Glover S. C. O., Klessen R. S., 2008, *ApJ*, 672, 757  
 Cowie L. L., McKee C. F., 1977, *ApJ*, 211, 135  
 Ehlervová S., Palouš J., Theis Ch., Hensler G., 1997, *A&A*, 328, 121  
 Elmegreen B. G., 1994, *ApJ*, 427, 384  
 Elmegreen B. G., 1998, in Woodward C. E., Shull J. M., Thronson H. A., Jr, eds, *ASP Conf. Ser. Vol. 148, Origins. Astron. Soc. Pac.*, San Francisco, p. 150  
 Elmegreen B. G., Palouš J., Ehlervová S., 2002, *MNRAS*, 334, 693  
 Ferrara A., 1998, *ApJ*, 499, L17  
 Field G. B., 1965, *ApJ*, 142, 531  
 Galli D., Palla F., 1998, *A&A*, 335, 403  
 Galli D., Palla F., 2002, *Planet. Space Sci.*, 50, 1197  
 Glover S. C. O., Jappsen A.-K., 2007, *ApJ*, 666, 1  
 Glover S. C. O., Abel T., 2008, *MNRAS*, 388, 1627  
 Greif T. H., Johnson J. L., Bromm V., Klessen R. S., 2007, *ApJ*, 670, 1  
 Greif T. H., Johnson J. L., Klessen R. S., Bromm V., 2008, *MNRAS*, 387, 1021  
 Haiman Z., Rees M. J., Loeb A., 1997, *ApJ*, 476, 458  
 Haiman Z., Abel T., Rees M. J., 2000, *ApJ*, 534, 11  
 Heger A., Woosley S. E., 2002, *ApJ*, 567, 532  
 Hollenbach D., McKee C. F., 1979, *ApJS*, 41, 555  
 Hollenbach D., McKee C. F., 1989, *ApJS*, 342, 306  
 Hosokawa T., Inutsuka S., 2006, *ApJ*, 646, 240  
 Johnson J. L., Greif T. H., Bromm V., 2008, *MNRAS*, 388, 26  
 Kitayama T., Yoshida N., 2005, *ApJ*, 630, 675  
 Kitayama T., Yoshida N., Susa H., Umemura M., 2004, *ApJ*, 613, 631  
 Koyama H., Inutsuka S., 2002, *ApJ*, 564, L97  
 Machida M. N., Tomisaka K., Nakamura F., Fujimoto M. Y., 2005, *ApJ*, 622, 39  
 Mac Low M.-M., Norman M. L., 1993, *ApJ*, 407, 207  
 Mackey J., Bromm V., Hernquist L., 2003, *ApJ*, 586, 1  
 McKee, C. F., Ostriker, J. P., 1977, *ApJ*, 218, 148

- Miyama S. M., Narita S., Hayashi C., 1987, *Prog. Theor. Phys.*, 78, 1273
- Nagakura T., Omukai K., 2005, *MNRAS*, 364, 1378
- Nakamura F., Umemura M., 2001, *ApJ*, 548, 19
- Nakamura F., Umemura M., 2002, *ApJ*, 569, 549
- Nahar S. N., Pradhan A. K., 1997, *ApJS*, 111, 339
- Nishi R., 1992, *Progr. Theor. Phys.*, 87, 347
- Nozawa T., Kozasa T., Umeda H., Maeda K., Nomoto K., 2003, *ApJ*, 598, 785
- Nozawa T., Kozasa T., Habe A., Dwek E., Umeda H., Tominaga N., Maeda K., Nomoto K., 2007, *ApJ*, 666, 955
- Omukai K., Palla F., 2003, *ApJ*, 589, 677
- Omukai K., Tsuribe T., Schneider R., Ferrara A., 2005, *ApJ*, 626, 627
- O'Shea B. W., McKee C. F., Heger A., Abel T., 2008, in O'Shea B. W., Heger A., Abel T., eds. *Proc. AIP Conf. Vol. 990, First Stars III. Am. Inst. Phys.*, New York, p. xiii
- Padmanabhan T., 1993, *Structure Formation in the Universe. Cambridge Univ. Press, Cambridge*
- Palla F., Salpeter E. E., Stahler S. W., 1983, *ApJ*, 271, 632
- Parker E. N., 1953, *ApJ*, 117, 431
- Salvaterra R., Ferrara A., Schneider R., 2004, *New Astron.*, 10, 113
- Schneider R., Ferrara A., Natarajan P., Omukai K., 2002, *ApJ*, 571, 30
- Schneider R., Ferrara A., Salvaterra R., 2004, *MNRAS*, 351, 1379
- Schneider R., Omukai K., Inoue A. K., Ferrara A., 2006, *MNRAS*, 369, 1437
- Shapiro P. R., Kang H., 1987, *ApJ*, 318, 32
- Spergel D. N., et al., 2003, *ApJS*, 148, 175
- Spitzer L., 1962, *Physics of Fully Ionized Gasses*, 2nd edn. Interscience, New York
- Stancil P. C., Lepp S., Dalgarno A., 1998, *ApJ*, 509, 1
- Stancil P. C., Schultz D. R., Kimura M., Gu J.-P., Hirsch G., Buenker R. J., 1999, *A&AS*, 140, 225
- Sutherland R. S., Dopita M. A., 1993, *ApJS*, 88, 253
- Thornton K., Gaudlitz M., Janka H.-T., Steinmetz M., 1998, *ApJ*, 500, 95
- Todini P., Ferrara A., 2001, *MNRAS*, 325, 726
- Tsuribe T., Omukai K., 2006, *ApJ*, 642, L61
- Tsuribe T., Omukai K., 2008, *ApJ*, 676, L45
- Uehara H., Inutsuka S., 2000, *ApJ*, 531, L91
- Umeda H., Nomoto K., 2002, *ApJ*, 565, 385
- van Leer B., 1979, *J. Comput. Phys.*, 32, 101
- Vasiliev E. O., Vorobyov E. I., Shchekinov Y. A., 2008, *A&A*, 489, 505
- Vishniac E. T., 1983, *ApJ*, 274, 152
- Whalen D., Abel T., Norman M. L., 2004, 610, 14
- Whalen D., Norman M. L., 2008, *ApJ*, 673, 664
- Whalen D., van Veelen B., O'Shea B. W., Norman M. L., 2008, *ApJ*, 682, 49
- Wise J. H., Abel T., 2007, *ApJ*, 665, 899
- Whitworth A. P., Bhattal A. S., Chapman S. J., Disney M. J., Turner J. A., 1994, *A&A*, 290, 421
- Yoshida N., Omukai K., Hernquist L., Abel T., 2006, 652, 6
- Yoshida N., Oh S. P., Kitayama T., Hernquist L., 2007, *ApJ*, 663, 687
- Yoshida T., Habe A., 1992, *Progr. Theor. Phys.*, 88, 251

**APPENDIX A: CHEMICAL REACTIONS**

We list the chemical reactions we include in Table A1.

The definitive version is available at [www.blackwellsynergy.com](http://www.blackwellsynergy.com).

Number	Reactions	References
R1	$\text{H} + \text{e}^- \rightarrow \text{H}^+ + 2 \text{e}^-$	1
R2	$\text{H}^+ + \text{e}^- \rightarrow \text{H} + \gamma$	1
R3	$\text{He} + \text{e}^- \rightarrow \text{He}^+ + 2 \text{e}^-$	1
R4	$\text{He}^+ + \text{e}^- \rightarrow \text{He} + \gamma$	2
R5	$\text{He}^+ + \text{e}^- \rightarrow \text{He}^{++} + 2\text{e}^-$	1
R6	$\text{He}^{++} + \text{e}^- \rightarrow \text{He}^+ + \gamma$	2
R7	$\text{H} + \text{e}^- \rightarrow \text{H}^- + \gamma$	2
R8	$\text{H} + \text{H}^- \rightarrow \text{H}_2 + \text{e}^-$	2
R9	$\text{H} + \text{H}^+ \rightarrow \text{H}_2^+ + \gamma$	2
R10	$\text{H}_2^+ + \text{H} \rightarrow \text{H}_2^* + \text{H}^+$	2
R11	$\text{H}_2 + \text{H}^+ \rightarrow \text{H}_2^+ + \text{H}$	2
R12	$\text{H}_2 + \text{e}^- \rightarrow 2\text{H} + \text{e}^-$	1
R13	$\text{H}_2 + \text{H} \rightarrow 3\text{H}$	3
R14	$\text{H}^- + \text{e}^- \rightarrow \text{H} + 2\text{e}^-$	1
R15	$\text{H}^- + \text{H} \rightarrow 2\text{H} + \text{e}^-$	1
R16	$\text{H}^- + \text{H}^+ \rightarrow 2\text{H}$	2
R17	$\text{H}^- + \text{H}^+ \rightarrow \text{H}_2^+ + \text{e}^-$	2
R18	$\text{H}_2^+ + \text{e}^- \rightarrow 2\text{H}$	2
R19	$\text{H}_2^+ + \text{H}^- \rightarrow \text{H} + \text{H}_2$	1
R20	$\text{D}^+ + \text{e}^- \rightarrow \text{D} + \gamma$	4
R21	$\text{D} + \text{H}^+ \rightarrow \text{D}^+ + \text{H}$	4
R22	$\text{D}^+ + \text{H} \rightarrow \text{D} + \text{H}^+$	4
R23	$\text{D} + \text{H} \rightarrow \text{HD} + \gamma$	4
R24	$\text{D} + \text{H}_2 \rightarrow \text{H} + \text{HD}$	4
R25	$\text{HD}^+ + \text{H} \rightarrow \text{H}^+ + \text{HD}$	4
R26	$\text{D}^+ + \text{H}_2 \rightarrow \text{H}^+ + \text{HD}$	5
R27	$\text{HD} + \text{H} \rightarrow \text{H}_2 + \text{D}$	4
R28	$\text{HD} + \text{H}^+ \rightarrow \text{H}_2 + \text{D}^+$	5
R29	$\text{D} + \text{H}^+ \rightarrow \text{HD}^+ + \gamma$	4
R30	$\text{D}^+ + \text{H} \rightarrow \text{HD}^+ + \gamma$	4
R31	$\text{HD}^+ + \text{e}^- \rightarrow \text{H} + \text{D}$	4
R32	$\text{D} + \text{e}^- \rightarrow \text{D}^- + \gamma$	2
R33	$\text{D}^+ + \text{D}^- \rightarrow 2\text{D}$	2
R34	$\text{H}^+ + \text{D}^- \rightarrow \text{D} + \text{H}$	2
R35	$\text{H}^- + \text{D} \rightarrow \text{H} + \text{D}^-$	2
R36	$\text{D}^- + \text{H} \rightarrow \text{D} + \text{H}^-$	2
R37	$\text{D}^- + \text{H} \rightarrow \text{HD} + \text{e}^-$	2
R38	$\text{H} + \text{H} + \text{H} \rightarrow \text{H}_2 + \text{H}$	6,7
R39	$\text{H} + \text{H} + \text{H}_2 \rightarrow \text{H}_2 + \text{H}_2$	6
R40	$\text{H}_2 + \text{H}_2 \rightarrow \text{H} + \text{H} + \text{H}_2$	3,6
R41	$\text{H} + \text{H} \rightarrow \text{H}^+ + \text{e}^- + \text{H}$	6
R42	$\text{C}^+ + \text{e}^- \rightarrow \text{C} + \gamma$	7
R43	$\text{O}^+ + \text{e}^- \rightarrow \text{O} + \gamma$	8
R44	$\text{O}^+ + \text{H} \rightarrow \text{H}^+ + \text{O}$	7
R45	$\text{O} + \text{H}^+ \rightarrow \text{O}^+ + \text{H}$	7
R46	$\text{He} + \text{H}^+ \rightarrow \text{He}^+ + \text{H}$	2
R47	$\text{He}^+ + \text{H} \rightarrow \text{He} + \text{H}^+$	2
R48	$\text{He} + \text{H}^+ \rightarrow \text{HeH}^+ + \gamma$	2
R49	$\text{He} + \text{H}^+ \rightarrow \text{HeH}^+ + \gamma$	2
R50	$\text{He} + \text{H}_2^+ \rightarrow \text{HeH}^+ + \text{H}$	2
R51	$\text{He}^+ + \text{H} \rightarrow \text{HeH}^+ + \gamma$	2
R52	$\text{HeH}^+ + \text{H} \rightarrow \text{He} + \text{H}_2^+$	2
R53	$\text{HeH}^+ + \text{e}^- \rightarrow \text{He} + \text{H}$	2

**Table A1.** References.—1. Abel et al. (1997); 2. Galli & Palla (1998); 3. Shapiro & Kang (1987); 4. Stancil, Lepp, & Dalgarno (1998); 5. Galli & Palla (2002); 6. Palla, Salpeter & Stahler (1983); 7. Stancil et al. (1999); 8. Nahar & Pradhan (1997).